The Influence of Amino Acid Protonation States on Molecular Dynamics Simulations of the Bacterial Porin OmpF

Sameer Varma,*†§ See-Wing Chiu,†§ and Eric Jakobsson*†‡§¶

*Center for Biophysics and Computational Biology, †National Center for Supercomputing Applications, ‡Department of Biochemistry, §Department of Molecular and Integrative Physiology, and ¶Beckman Institute for Advanced Science and Technology, University of Illinois at Urbana-Champaign, Urbana, Illinois 61801

ABSTRACT Several groups, including our own, have found molecular dynamics (MD) calculations to result in the size of the pore of an outer membrane bacterial porin, OmpF, to be reduced relative to its size in the x-ray crystal structure. At the narrowest portion of its pore, loop L3 was found to move toward the opposite face of the pore, resulting in decreasing the cross-section area by a factor of ~2. In an earlier work, we computed the protonation states of titratable residues for this system and obtained values different from those that had been used in previous MD simulations. Here, we show that MD simulations carried out with these recently computed protonation states accurately reproduce the cross-sectional area profile of the channel lumen in agreement with the x-ray structure. Our calculations include the investigation of the effect of assigning different protonation states to the one residue, D^{127}, whose protonation state could not be modeled in our earlier calculation. We found that both assumptions of charge states for D^{127} reproduced the lumen size profile of the x-ray structure. We also found that the charged state of D^{127} had a higher degree of hydration and it induced greater mobility of polar side chains in its vicinity, indicating that the apparent polarizability of the D^{127} microenvironment is a function of the D^{127} protonation state.

INTRODUCTION

OmpF, located in the outer membrane of Gram-negative bacteria, belongs to a family of channel proteins that facilitate uptake of nutrients. Under normal conditions, it associates with other OmpFs in the membrane and exists as homotrimers (for reviews, refer to (1–8)). Each monomer folds into a rigid 16-stranded β-barrel with eight turns at the periplasmic side and eight loops (L1–L8) that narrow the structure at the cell surface and channel interior (9). Loop L3 in particular folds inside the barrel and creates a narrow region halfway through the membrane. This region, also called the ''constriction zone'', gives the pore an hourglass-like shape.

OmpF allows diffusion of ions and even larger molecules of the size of several hundred daltons. It is moderately selective toward cations and has also been found to be voltage sensitive. Although several theoretical and experimental studies have been conducted to elucidate the origins of these observed behaviors, they are still not clearly understood. Molecular dynamics (MD) provides for an excellent tool to investigate these channel properties at the microscopic level. However, all the MD trajectories reported previously (10–12) have resulted in producing large deviations of the trimer from its x-ray crystal structure, specifically at the constriction zone of the channel. In the constriction zone, loop L3 was found to move into the permeation pathway of the channel and toward the opposite face of the pore. In all these simulations, this movement of loop L3 was to an extent that it had decreased the cross-sectional area of the constriction zone to ~½ its magnitude in the x-ray structure. The low temperature (77 K) crystal structure indicates the dimensions of the constriction zone to be 7×11 Å, which corresponds to a solvent accessible area of ~32 $Å^2$ (9). In the trajectory generated by Im and Roux (11), this area had decreased to ~15 $Å^2$, and in the trajectory generated by our group (12), this area had decreased to ~19 $Å^2$. Such a decrease in the size of the narrowest region of the pore can have substantial effects on permeation properties inferred from these simulations, especially since this region of the pore is exposed to several charged residues. The assumption here, that the size of the constriction zone as inferred from the low temperature crystal structure indeed corresponds to the size of the functional channel in its open state, has been validated by several experimental studies (1,13,14).

We had previously hypothesized (15) that the structural deviation in the constriction zone of the channel seen in MD simulations may have been due to protonation states assigned to some specific titratable residues lining the lumen of the channel and had therefore remodeled the protonation states of these titratable residues using Poisson-Boltzmann theory and taking into account the interactions of charged residues. Our results suggested a different set of protonation states from all of the previous assumptions (10,11,16) and left one ambiguity. Residue D^{127} was found to have a higher probability of being protonated if electrostatic pKa calculations were performed using a protein dielectric constant <12. On the other hand, if we assumed a protein dielectric constant of 12 or higher, as also used by Alcaraz et al. (17), this residue was found to have a higher probability of being fully charged. The results of the protonation calculations on

Submitted April 26, 2005, and accepted for publication August 22, 2005.

Address reprint requests to Eric Jakobsson, Tel.: 217-244-2896; Fax: 217-244-2909; E-mail: jake@ncsa.uiuc.edu.

© 2006 by the Biophysical Society

0006-3495/06/01/112/12 $2.00

doi: 10.1529/biophysj.105.059329

D^{127} raise the following issues: Which protonation state assignment is the correct one? Conversely, which assignment of dielectric constant for the protein is the correct one?

In the crystal structure, the side chain of D^{127} interacts with two resolved water molecules that are contiguous with bulk water and also with several other residues, notably V^{130}, R^{167}, Q^{200}, Q^{213}, and A^{237} (see Fig. 6). It could be termed partially buried in a polar environment. In that context, the issue of the D^{127} protonation state is related to the issue of the energetic cost of burying a charged residue, or of charging a buried residue. Experimental pKa shifts associated with burying charged residues seem more consistent with treating such cases by assuming a higher polarizability (18–21), which may be either due to increased penetration of water in the cavity or the intrinsic ability of the local environment of the protein to respond to changes in protonation state via disorder or rearrangement. Recent experimental work designed to distinguish between these two phenomena (local disordering or increased water penetration) in nonpolar cavities suggests local disordering as the actual mechanism, at least in the particular systems explored (22–24).

In this work, we generate and analyze data from two separate 9-ns-long MD trajectories of the trimer (embedded in explicit POPE bilayers and 1 M KCl salt solutions) differing only in the protonation state of residue D^{127}. This work has two aims: a), to test our hypothesis that assignments of protonation states to specific titratable residues was the problem in earlier MD simulations, and b), to explore the consequences of varying the protonation state of D^{127}.

METHODS

Under Methods we present three sections: ''Assigning protonation states to titratable residues'', ''Molecular dynamics'', and ''Calculating solvent accessible cross-sectional areas''. All simulations for this work were conducted on the IA-32 Linux cluster provided by the National Center for Supercomputing Applications, University of Illinois, Urbana-Champaign.

Assigning protonation states to titratable residues

Protonation states of all titratable residues lining the lumen of the channel were assigned values based on our earlier work (15). Residues E^{296} and D^{312} were assigned protonation states to conform to the hydrogen bond network indicated by Fig. 4 *c* in that publication. All other residues were assigned protonation states corresponding to their default values at neutral pH.

Molecular dynamics

All energy minimizations and MD simulations were carried out using the GROMACS (Ver. 3.1.4) modeling software (25).

Initially, a small POPE lipid bilayer containing 128 lipid molecules and 28 waters per lipid molecule was constructed and equilibrated at 310 K for 10 ns. A larger POPE bilayer (1152 POPE + 32,256 waters) was then constructed by multiplying the last snapshot of the MD trajectory using the GROMACS utility program — *genconf*. This large POPE bilayer was then subjected to an equilibration for 1 ns at the same temperature. The last snapshot of this MD trajectory was then used for solvating the two OmpF trimers. In a separate setup, each trimer was rotated to orient its central axis parallel to that of the bilayer normal (*z* axis). The coordinates of the trimer were then translated to the center of a box that had XY dimensions the same as that of the lipid bilayer system (18 nm × 18 nm). Each of the trimers was then embedded in separate equilibrated lipid bilayer systems by using the GROMACS utility program — *genbox*. The *z* coordinates of the geometric centers of the trimers and their respective bilayers were then manually superimposed. The entire system, now comprising the lipid bilayer, water, and protein, was then energy minimized with position restraints on all protein atoms. The system was then translated to the center of a larger box (dimensions, 18 nm × 18 nm × 10 nm) and then solvated with more water. To generate a KCl solvent having a 1 M ionic strength, 2 out of every 57 water molecules were randomly selected and replaced by a set of K^+ and Cl^- ions. To obtain charge neutrality in the two trimer systems, one containing the residue D^{127} in its protonated state and the other containing the same residue in its deprotonated state, an additional 30 and 33 water molecules were respectively replaced by K^+ ions. Thus finally, the protonated D^{127} trimer system ended up embedded in a lipid bilayer having 787 POPE molecules, 59,707 water molecules, 1104 K^+ ions, and 1074 Cl^- ions, and the deprotonated D^{127} trimer system ended up embedded in a lipid bilayer with the same number of lipid molecules and Cl^- ions but 3 extra K^+ ions in place of 3 water molecules. Each of the OmpF trimer systems was then once again energy minimized with position restraints on all protein atoms. The MD trajectory was then initiated with harmonic restraints (force constant, 1000 kJ $mol^{-}nm^{-2}$) on all protein heavy atoms. These harmonic restraints were maintained for the first 500 ps, after which they were gradually reduced in steps of 100 kJ mol^{-1} nm^{-2}/50 ps. As a result, the first nanosecond trajectory was generated with harmonic restraints. Thereafter, the two systems were simulated without any restraints for another 8 ns. The system size was continuously monitored to obtain the optimal point in time for data analysis. We found that the simulation box sizes stabilized near the 3 ns mark. Thus, all the data for this manuscript were collected and analyzed after the 3 ns mark.

For each of these simulations we used normal pressure temperature conditions with semiisotropic pressure coupling; particle mesh Ewald with Fourier spacing of 0.15 nm, a sixth-order interpolation, and a 1.0 nm cutoff in direct space for long-range electrostatic corrections; a twin-range cutoff (1.0/1.6) for van der Waal interactions; a time step size of 2 fs; five step intervals for neighbor pair list updates; the LINCS algorithm (26) to constrain all bond lengths; the SETTLE algorithm (27) for constraining bond lengths in water molecules (SPC/E); a Nosé-Hoover algorithm (28) with a coupling constant of 0.2 ps to maintain temperature at 310 K; a Parrinello-Rahman method (29) with a coupling constant of 1 ps to maintain semiisotropic boundary pressure conditions; the GROMOS96 43A1 force field (30) for protein; and a recently revised force field parameter set for POPE lipid molecules (S. W. Chiu, E. Jakobsson, and H. L. Scott, unpublished). The newly calculated POPE force field parameter set is available as supplementary information to this work.

Calculating solvent accessible cross-sectional areas

The program HOLE (32) determines the dimensions of a pore running through a structural model of an ion channel. It does so by finding the best route for a sphere with variable radius that can squeeze through a channel. HOLE defines the axis of the channel as a series of points in which each point is the center of the largest sphere that can fit into the channel at each depth into the channel. HOLE, in its original form, also defines the channel cross-sectional area as the area of a circle whose radius is the same as the radius of the largest sphere. In a later HOLE refinement for the purpose of dealing with irregular channel shapes (33), the points on the channel axis are expanded into lines and the channel cross-sectional area is defined as the cross section in the plane perpendicular to the channel protein axis (also corresponding to the mean membrane plane) of spherocylindrical capsules expanded from the lines. In our methodology we use the spherical HOLE routine of the channel to define a set of points, which we call $\{r_i\}$ (where each point r_i is the center of the pore at some position along the path of the

pore). But to most accurately characterize the cross section for channels of highly irregular geometry, we use the following angular-sweep methodology in conjugation with the HOLE (33) algorithm:

From each point r_i at the center of the channel as defined by HOLE, we send out a set of ''rays'' in the plane perpendicular to the long axis of the protein. Each ray terminates when it arrives at a point 1.4 Å (the radius of a water molecule) from the van der Waals surface of any protein atom, defining a vector. Each vector has a length R^i_θ where the superscript i denotes the depth of the plane into the channel and the subscript θ denotes the angular direction of the ray. If the rays are sent out at radial intervals of $\Delta\theta$ radians, then for sufficiently small $\Delta\theta$ the cross-sectional area of the channel at the depth i is given very accurately by the assumption that the cross section is tiled with $2\pi/\Delta\theta$ ''pie-wedges'', each with an area of $1/2(R^i_\theta)^2\Delta\theta$. Thus the solvent accessible cross-sectional area at depth i ($SAXA_i$) is given by

$$SAXA_i = \frac{1}{2}\sum_{\theta=0}^{2\pi-\Delta\theta}\left(R^i_\theta\right)^2\Delta\theta. \quad (1)$$

The method is shown graphically in Fig. 1. In our calculations for this work, we chose $\Delta\theta$ to be 0.02 radians.

RESULTS AND DISCUSSIONS

We generated two separate 9-ns-long MD trajectories of the trimer embedded in explicit POPE bilayers and 1 M KCl salt solutions, each containing approximately a quarter of a million atoms. The first 3 ns of each trajectory were considered equilibration and excluded from data analysis. The starting conditions of these trajectories essentially differ from each other only in the assignment of the protonation state of residue D^{127}. We present and discuss results in three sections below: ''Backbone structure and dynamics'', ''Side-chain configurations and hydrogen-bonding patterns'', and ''Ion permeation''.

Backbone structure and dynamics

The backbone structure of each monomer of OmpF can be described (10) as a 16-stranded antiparallel β-barrel enclosing an aqueous pore. The β-strands are connected via eight β-hairpin turns (T1–T8) at the periplasmic side and eight loops (L1–L8) at the extracellular side of the channel. All the periplasmic turns are short and comprise 2–4 residues with the exception of turn T4, which comprises nine residues. In contrast, the loops are longer and their lengths vary from 7 residues (L7) to 35 residues (L3). Six of these loops, L1 and L4–L8, extend toward the axis of the β-barrel and decrease the size of the pore at the extracellular end. Loop L2, also called the latching loop, extends away from the axis of its pore and folds into the channel of an adjacent monomer. Loop L3 folds into the channel pore and packs against the channel wall, decreasing the size of the pore halfway through the length of the channel. This gives the pore an hourglass-like shape, with the narrowest region of the pore (also referred to as the constriction zone) having a solvent accessible cross-sectional area (SAXA) of ~32 $Å^2$.

In both the MD trajectories generated here, we find that the secondary structure of each monomer, as revealed by the x-ray structure, is maintained. We also find that in both simulations, the backbones of all the extracellular loops and the periplasmic turns are more flexible than the transmembrane β-barrel. This can be seen in Fig. 2, which compares the averages of the backbone root mean-square (RMS) fluctuations of the three monomers computed from these MD trajectories and those derived from Debye-Waller B-factors. We find that the computed RMS fluctuations of all the loops and extracellular turns in both simulations are either in accord with, or slightly greater than, those derived from the experimental B-factors. The larger fluctuations of some of these loops and turns may be due to the differences between the crystallization and simulation conditions. OmpF was crystallized at a temperature of 77 K and in the absence of any salt (34), whereas these simulations were performed at temperatures of 310 K and in the presence of 1 M salt solutions.

Residue D^{127} is located near the extracellular end of the pore in loop L3 and interacts with residues belonging to three

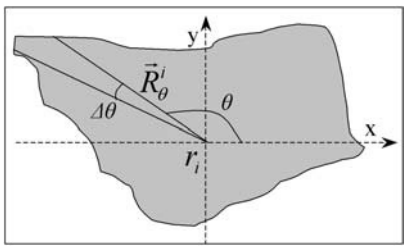

FIGURE 1 Schematic of the angular-sweep methodology that was used in conjugation with the HOLE (33) algorithm to determine accurate descriptions of SAXA of channel pores. See the ''Calculating solvent accessible cross-sectional areas'' section for details. The magnitude of $\Delta\theta$ as appears in the schematic is set large only for the purpose of visualization. It was set at a value of 0.02 radians for computation purposes.

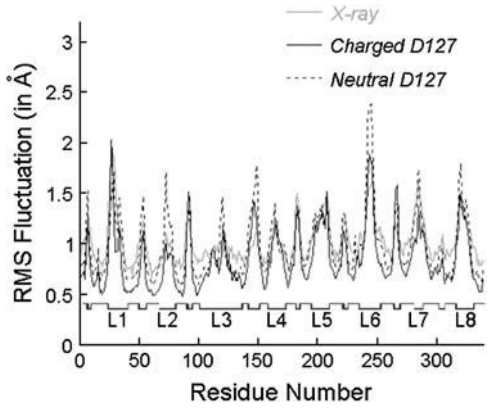

FIGURE 2 MD backbone RMS fluctuations of OmpF simulated with D^{127} in its charged and neutral states are compared with RMS fluctuations derived from Debye-Waller B-factors. The RMS fluctuations were calculated for all three monomers of each trimer and then averaged to obtain a single representative profile for each trimer. The B-factors derived from the crystal structure were converted into RMS fluctuations using the formula $\text{rmsf} = \sqrt{3B/8\pi^2}$.

other loops: R^{167} in L4, Q^{200} and Q^{213} in L5, and A^{237} in L6. A comparison of the RMS fluctuation profiles computed from the two present simulations, which essentially differ from each other only in the protonation state of D^{127}, indicates no systematic effects of the protonation state of residue D^{127} on backbone fluctuations of loops L4 and L5. For loop L6, we find that the RMS fluctuations are larger when D^{127} is set neutral. Based on the crystal structure, the carboxylate side chain of D^{127} in loop L3 is expected to interact with the backbone carbonyl group of residue A^{237} in loop L6. We show later (in Fig. 11) that the distance between the carboxylate side chain of D^{127} and the carbonyl oxygen of A^{237} undergoes lesser fluctuations if D^{127} is set neutral. Therefore, the larger RMS fluctuations of loop L6 seen in the case of a neutral D^{127} are not likely to be due to the protonation state assigned to D^{127}.

Table 1 lists the average RMS deviations for the backbone atoms of all the eight loops and the longest turn (T4) for each of the three monomers simulated in the two trajectories. We see that there are no systematic effects of the protonation state of D^{127} on the RMS deviations of these loops. We also find that some loops, notably loop L1 in monomer M1 and loop L8 in monomer M3 of trajectory generated with a charged D^{127}, have exceptionally much higher RMS deviations than all the other loops. These are, however, sporadic events but indicate that loops L1 and L8 are flexible and can adopt multiple conformations, especially since they are all made up of several polar residues. The time-averaged MD structures of these two loops are shown superimposed on the crystal structure in Fig. 3.

Together, we find that the assignment of a protonation state to residue D^{127} does not have any systematic effects on the structure or the dynamics of the protein backbone. We also find that irrespective of the assignment of the protonation state to residue D^{127}, the protein backbone does not undergo any major systematic conformational changes during the simulation. This result is, however, different from that obtained from any of the previously reported MD simulations (10–12), mainly with respect to the average structure of the PEFGGD fragment of loop L3. The PEFGGD fragment of loop L3, which comprises residues P^{116}, E^{117}, F^{118}, G^{119}, G^{120}, and D^{121} at the tip of the loop, is the signature sequence of enterobactrial porins (35). It is shown in Fig. 3, highlighted orange in the x-ray structure. In Fig. 3, we also see that in the current two simulations, there are no systematic differences between the average structures of these fragments in any of the monomers of the two trimers. However, in all previous MD simulations, this fragment was consistently found to move into the permeation pathway and toward the opposite face of the pore, decreasing the SAXA of the narrowest region of the constriction zone to almost one-half the corresponding magnitude in the x-ray structure. In the trajectory generated by Im and Roux (11), the SAXA of the narrowest portion of the constriction zone had decreased from ~32 $Å^2$ to ~15 $Å^2$, and in the trajectory generated by our group (12), this area had decreased to ~19 $Å^2$. In this simulation, we do not see such a decrease in the size of the constriction zone. This is more evident from Fig. 4, which shows the variation of SAXA along the axes of the pores in the time-averaged MD structures of each of these simulations in comparison with the variation of the SAXA

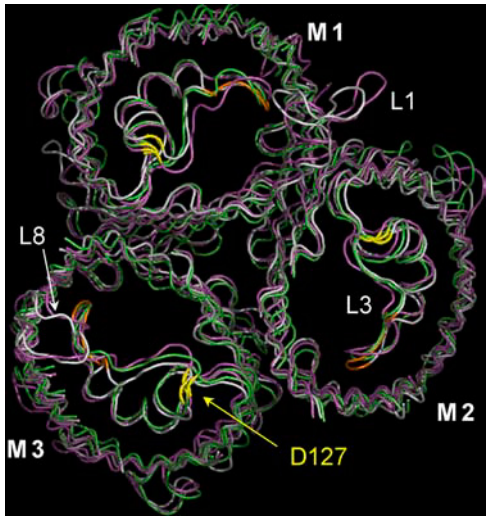

FIGURE 3 Superimposed backbone structures of OmpF. The time-averaged MD structures of the trajectories generated with a charged D^{127} (*magenta*) and with a neutral D^{127} (*green*) are shown superimposed on the x-ray structure. Most of the loops have been clipped to clearly show the structures of the following loops: loops L3 in all trimers, loops L1 of monomer M1 in the x-ray structure and in the average structure of trajectory generated with a charged D^{127}, and loops L8 of monomer M3 in the x-ray structure and in the average structure of trajectory generated with a charged D^{127}. The backbone atoms of residue D^{127} are highlighted in yellow. The backbone atoms of the PEFGGD fragments in loops L3 (*tip* of the loop), which were found to move toward the opposite face of the pore in all previous simulations, are highlighted in orange in the x-ray structure. This figure was created using PyMOL (http://pymol.sourceforge.net).

TABLE 1 Comparison of average RMS deviations of backbone atoms of different residue fragments of each monomer (M1, M2, and M3) in the two trimers simulated using different protonation states for residue D^{127}

Residue fragment		RMS deviation (in Å)					
		Charged D^{127}			Neutral D^{127}		
		M1	M2	M3	M1	M2	M3
1–340	All	1.8	1.4	1.5	1.5	1.5	1.4
24–39	L1	2.7	1.3	1.4	1.3	1.0	1.7
67–79	L2	1.3	0.9	1.6	1.2	1.7	0.9
101–135	L3	1.3	1.0	1.1	1.2	1.2	1.3
159–172	L4	0.6	1.0	0.5	0.7	0.7	0.6
196–209	L5	0.7	1.1	1.2	0.9	0.9	1.0
236–252	L6	0.7	1.0	1.1	0.9	1.1	1.0
282–288	L7	0.6	0.4	0.4	0.4	0.7	0.4
317–330	L8	1.1	1.1	1.9	1.1	1.1	1.3
142–150	T4	0.4	0.4	0.4	0.4	0.4	0.3

The fragments labeled L1–L8 are the extracellular loops, and the fragment labeled T4 is the longest periplasmic turn.

along the axis of the pore in the x-ray structure (refer to the Methods section for calculation details). In this figure, we also show for comparison the SAXA profile for the mean structure from our own previous MD simulation (12). Clearly in the current two simulations, we find that size of the constriction zone does not decrease dramatically, in contrast to previous simulations.

The x-ray structure (9) indicates that the PEFGGD fragment of loop L3 is expected to interact with the wall of the β-barrel via a hydrogen bond network involving the backbone nitrogen atom of residue E^{117} and two other titratable residues, E^{296} and D^{312}. This is shown in Fig. 5. The differences between the current MD data and data from all previous MD simulations, therefore, appear to arise from differences in the assignments of the protonation states of residues D^{312} and E^{296}. In two of the previous simulations (10,11), both residues were set protonated. In the other simulation (12), both residues were set partially charged. The spatial proximity of residues D^{312} and E^{296} in this structure suggests that at least one of the two acidic groups should be protonated. If D^{312} is protonated, the hydrogen bonding between the carboxylate group of D^{312} and the backbone nitrogen of E^{117} is weakened. This seems likely to have caused the large-scale deviations of the loop from the crystal structure in two of the previous simulations (10,11). This interpretation of the significance of the charged state of D^{312} is supported by the work of Liu and Delcour (36), who mutated residue D^{315} in OmpC (which corresponds to aspartate D^{312} in OmpF) to an uncharged alanine. This mutation essentially mimics a scenario in which residue D^{312} is assumed protonated and thereby incapable of forming a hydrogen bond with the backbone nitrogen atom of residue E^{117}. They found that such a mutation resulted in a significant increase in the frequency of pore closures in patch clamp studies, clearly demonstrating the significance of the charged state of residue D^{312} in maintaining both the structural and functional properties of the channel. It should be noted that although this correlation between a particular experimental condition and a previous computational setup neatly demonstrates the effect of discharging residue D^{312}, it does not necessarily imply that a change in the charged state of D^{312} is a trigger for voltage gating in the native channel. The involvement of loop L3 in voltage gating via its movement into the permeation pathway was ruled out by a cysteine-scanning mutagenesis investigation (37).

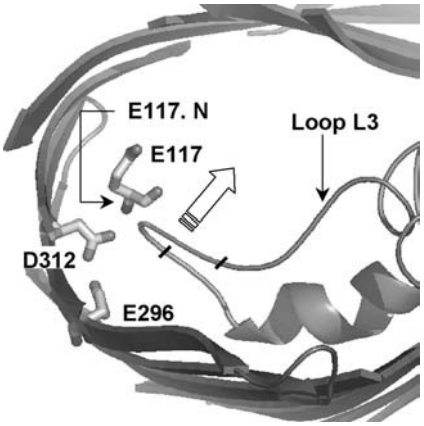

FIGURE 5 Partial view of the x-ray structure (9). Titratable residues E^{117}, E^{296}, and D^{312}, which are involved in the interaction of the PEFGGD fragment of loop L3 with the wall of the β-barrel, are shown as stick models. The solid lines on the backbone of loop L3 indicate the ends of the PEFGGD fragment. A block arrow indicates the direction of the movement of this fragment that was seen in all previous simulations. This figure was created using PyMOL (http://pymol.sourceforge.net).

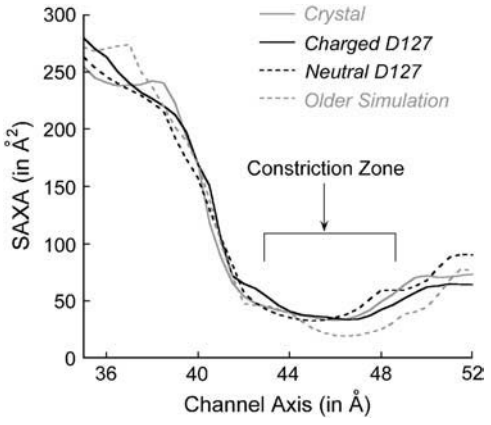

FIGURE 4 Variation of SAXA along the axis of four OmpF monomers: crystal structure, monomer representing the MD trajectory generated with a neutral D^{127}, monomer representing the MD trajectory generated with a charged D^{127}, and monomer representing the MD trajectory generated for a previous investigation with other charge assignments for the residues (12). The monomers used for generating SAXA profiles were obtained as follows. MD trajectories of the trimers simulated using different charge states of D^{127} and for a previous investigation were first separately aligned to obtain their respective average trimer structures. The three monomers in each trimer were then separately superimposed to obtain average monomer structures for each trajectory. These two monomers were then superimposed onto the crystal structure to eliminate any rotational artifacts in SAXA profiles. The SAXA profiles were then calculated using HOLE (33) along with an angular-sweep algorithm (see Methods for details).

On the other hand, setting E^{296} simultaneously charged along with D^{312}, as our group previously did (12), creates a strong electrostatic repulsion between the two acidic side chains triggering a coordinated movement of D^{312} along with the PEFGGD segment of loop L3 into the permeation pathway of the channel, essentially the same structural result as the other previous simulations but for a slightly different underlying reason. In the current simulation, D^{312} was set fully charged and E^{296} was set protonated based on our recent protonation state calculations (15). In this scenario, D^{312} acts as a proton acceptor from both residues, E^{117} and E^{296}, which keeps the segment tethered to the wall of the β-barrel in accord with the x-ray structure. In these simulations, we also note that the χ-angles of the side chain of residues E^{296} in the different monomers undergo rotations that result in minor coordinated movements of the side chains of

their respective D^{312} residues either toward or away from the wall of the β-barrel. These side-chain movements result in positioning PEFGGD fragments of loops L3 either slightly away from (monomers M2 of both trimers in Fig. 3) or slightly closer to (monomer M1 of the trimer simulated with a charged D^{127}) the wall of the β-barrel. However, such movements had no noticeable effect on the average SAXA profiles of the constriction zone.

In summary, a comparison of backbone RMS fluctuations and the backbone RMS deviations between the two trajectories showed no significant dissimilarities. This implies that the assignment of a protonation state to D^{127} does not have a large-scale effect on the structural dynamics of the trimer. In the following section, we explore the side-chain configurations and hydrogen-bonding patterns in the vicinity of D^{127} for both assumptions of protonation states.

Side-chain configurations and hydrogen-bonding patterns

Fig. 6 shows the local environment of residue D^{127} as revealed by the x-ray structure (9). There are two carbonyl oxygen atoms, A^{237}.O and Q^{213}.OE1 that are within 3.5 Å of the carboxylate group of D^{127}, indicating that they may be able to contribute to stabilization of D^{127} in its neutral (protonated) state. However, there are two crystallographically resolved water oxygens at distances 3.7 Å and 2.9 Å, respectively, from the OD1 and OD2 atoms of D^{127}, indicating that they may be able to stabilize D^{127} in its charged state. Furthermore, there are four amine groups, two belonging to R^{167} and one each belonging to residues Q^{200} and Q^{213}, that are close to ~6 Å from the carboxylate side chain of D^{127}, indicating that they may be able to further stabilize the charged state of D^{127}. Thus, the x-ray data do not provide unambiguous guidance to model the protonation state of D^{127}. Moreover, our previous electrostatics-based pKa calculations (15) predicted a protonation state of D^{127} that was dependent on the choice of the protein dielectric constant, further indicating a close balance between factors tending toward a neutral state and those tending toward a charged state. In essence, the presence of a charged arginine and several other protein dipoles and two water dipoles combine to put residue D^{127} in the center of a hydrogen bond network with a complicated balance of forces that on the face of it are consistent with either a charged or uncharged state for D^{127}.

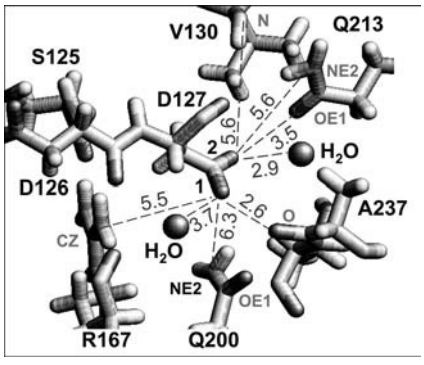

FIGURE 6 Local environment of residue D^{127} as revealed by the x-ray structure (9). Residue names are indicated in black, and the atom names are indicated in gray. Carboxylate oxygen atoms OD1 and OD2 of D^{127} are labeled as 1 and 2, respectively. Distances from these atoms to neighboring proton donors and acceptors, including the crystallographically resolved water oxygen atoms (labeled as H_2O), are indicated in angstrom units. This figure was created using RasMOL.

By contrast with D^{127}, the reasons our previous electrostatics-based pKa calculations predicted R^{167} to be fully charged are evident by inspection from its local environment. First, the side chain of R^{167} is not straight but bent toward its own backbone, such that its side-chain amine group is at hydrogen bonding distance from its own backbone oxygen atom. Second, there are two other carbonyl oxygens, one belonging to residue S^{125} and the other belonging to residue D^{126}, that are within hydrogen-accepting distances from R^{167} (also shown in Fig. 6). And third, R^{167} is not completely buried in the low dielectric environment of the protein, implying that associating a charge with R^{167} is electrostatically not expensive.

To investigate local effects of assigning a protonation state to residue D^{127}, we first computed the average center of mass deviations of all the residues involved in its hydrogen bond network, namely, D^{127}, V^{130}, R^{167}, Q^{213}, and A^{237} in both trajectories. The computed values of these deviations in all the six monomers are listed in Table 2. We find that R^{167} is a special case, because its center of mass deviation is exceptionally higher than all the other residues. Since the backbone atoms of R^{167} remain within 0.03 Å of the crystal structure, it follows that the relatively large center-of-mass deviation is entirely due to a side-chain configuration that is different from the crystal structure. Fig. 7 compares the time-dependent center-of-mass deviations of residue R^{167} for all monomers in the two trajectories. In the MD trajectory, when D^{127} was neutral, we find that the side chains of R^{167} of all monomers consistently move away from D^{127} and into the permeation pathway of the channel. We find that this

TABLE 2 Comparison of average center of mass deviations of all residues involved in the hydrogen bond network of residue D^{127}

	Average center of mass deviation (in Å)					
	Charged D^{127}			Neutral D^{127}		
Residue	M1	M2	M3	M1	M2	M3
D^{127}	0.49	0.52	0.53	0.78	0.76	0.63
V^{130}	0.44	0.46	0.42	0.38	0.43	0.43
R^{167}	1.30	1.11	0.70	1.33	1.40	1.34
Q^{200}	0.18	0.40	0.39	0.52	0.20	0.36
Q^{213}	0.52	0.27	0.27	0.64	0.44	0.46
A^{237}	0.45	0.12	0.22	0.10	0.11	0.09

The deviations of these residues belonging to each of the three monomers M1, M2, and M3 of the two simulated trimers are tabulated separately.

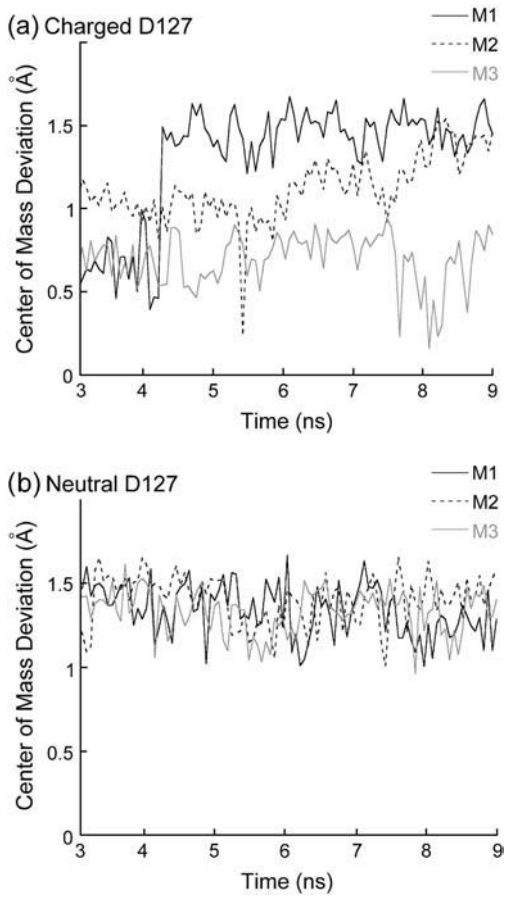

FIGURE 7 Time-dependent center of mass deviation from x-ray crystal structure of residue R^{167} belonging to each of the three monomers (M1, M2, and M3) of the trajectories generated with (*a*) a charged D^{127} and (*b*) a neutral D^{127}. These deviations were first computed at intervals of 5 ps, and then cubic spline interpolation was used to eliminate the noise in the data associated with rapid fluctuations.

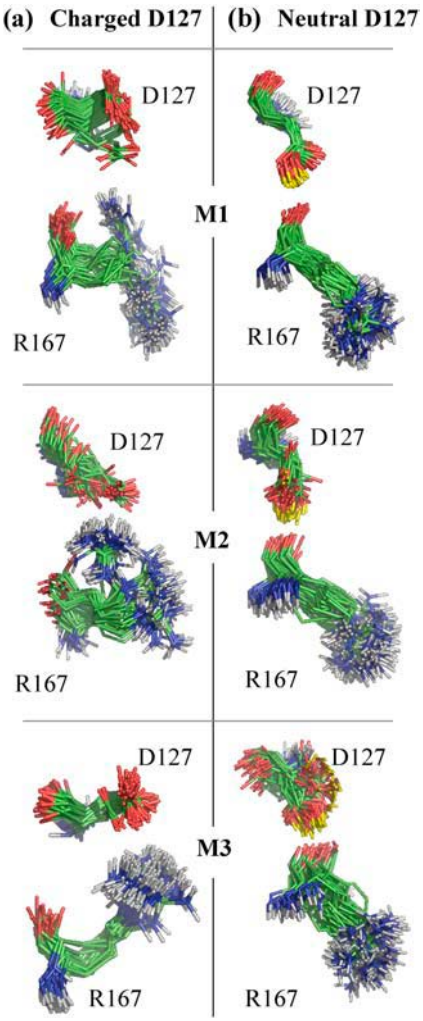

FIGURE 8 Conformational space sampled by residues D^{127} and R^{167} in each monomer (M1, M2, and M3) of the trajectory generated with D^{127} in its (*a*) charged state and (*b*) neutral state. The carbon atoms are shown in green, oxygen atoms in red, nitrogen atoms in blue, and the protons on the side-chain carboxylate groups in yellow. Note that the figures are drawn with slightly different perspectives to highlight the relative conformations of these residues. The backbone atoms of these residues essentially do not undergo any structural deviation (RMSD < 0.03 Å) and the apparent relative deviations are entirely due to side-chain reorientations. We find that the charged state of D^{127} does better at preventing the side chain of residue R^{167} from moving into the lumen of the channel. This figure were created using PyMOL (http://pymol.sourceforge.net).

side-chain movement occurs within the first 0.3 ns of the simulation conducted without any harmonic restraints. On the other hand, in the MD trajectory when D^{127} is charged, we did not find R^{167} to move away from D^{127} until the 3 ns mark. We found the same deviation in two out of the three monomers, M1 and M2, but only after 3 ns and 6 ns, respectively. Together, we find that the charged state of D^{127} shows a stronger tendency to hold the side chain of R^{167} out of the permeation pathway. This is illustrated in Fig. 8, where we compare the conformational space sampled by residues D^{127} and R^{167} in each of the three monomers of the two simulated trajectories. The side-chain configuration of R^{167} in monomer M3 with charged D^{127} is in agreement with the crystal structure.

Fig. 9, *a* and *b*, shows the radial distribution function of water oxygens around each of the carboxylate oxygens of residue D^{127} for the charged and neutral states, respectively. In the crystal structure, there are crystallographically resolved water molecules within hydrogen bonding distance from both the OD1 and OD2 atoms of D^{127}. In these simulations, it is seen that irrespective of the protonation state of residue D^{127}, a water molecule is consistently present at hydrogen bonding distance from the OD2 atom of D^{127}, consistent with the x-ray data. However, we find that a water molecule is present close to atom OD1 only when residue D^{127} is fully charged. We find that the water molecule that was crystallographically resolved near atom OD1 is missing in the trajectory of all the three monomers when residue D^{127} is neutral.

Recent work of Denisov et al. (23) suggests that water molecules resolved in nonpolar cavities using low temperature

x-ray crystallography are not likely to be immobilized (with dwell times <10 ns) under physiological conditions. Our simulations suggest the same in polar cavities, since we see multiple water molecules interacting with D^{127} during the course of the simulation for both of the assumed charged states. For instance, we find in the case of monomer M3 of the trimer simulated with a charged D^{127} six separate water molecules that move in and out of this cavity and interact with D^{127} at some point of their respective trajectories. This is illustrated in Fig. 10, which shows the positions visited over a 5 ns interval of each of the six water molecules that adopted the nearest neighbor position to the OD1 atom of D^{127} at any time during the 5 ns. This figure shows the water molecule positions at 50 ps intervals, so there are in principle 100 positions plotted for each water (although not all are visible, because some are hidden behind others). Interestingly, one of these water molecules (coded *yellow*) also translocated the channel between the periplasmic and extracellular ends.

The panels of Fig. 11 show the time evolution of the relative interatomic distances shown in Fig. 6 that are not considered in Figs. 7–9. Overall, Fig. 11 reveals distinct differences in side-chain behavior as a function of whether or not D^{127} is protonated. In the neutral state, the interatomic distances move to distinctly larger values than seen in the crystal structure and then mostly remain near the same values for the rest of the duration of the simulation. In the charged state, the interatomic distances remain relatively closer to the crystal structure values than for the protonated state but continue to undergo transitions during the rest of the duration of the simulation. Note that these changes are all side chain changes. Note also that the simulations are done at 310 K and the x-ray structure was determined at 77 K. It appears that at physiological temperatures the side chains in the vicinity of D^{127} find conformations that tend to increase the interatomic distance of electrostatically interacting side chain atoms, as compared to the crystal structure. This tendency is especially pronounced when D^{127} is in its neutral state. For both the neutral and charged states, this ''expansionist'' tendency of the side chains occurs in the context of a mean backbone structure that remains essentially fixed at the crystal structure. Presumably such an ''expansion'' in the context of an unchanging backbone structure can only occur near the surface of a protein, since in the core there would be no room to expand.

The increased frequency of side-chain transitions in the vicinity of the charged D^{127} suggests that the apparent polarizability of the protein in the vicinity of the charged D^{127} is higher than in the vicinity of the uncharged D^{127}. Interestingly, this was also seen in the experimental work of Denisov et al. (23) in nonpolar cavities.

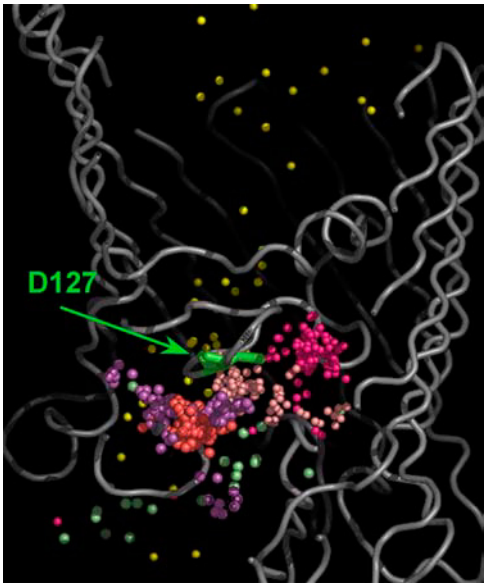

FIGURE 10 Superimposed trajectories of six separate water molecules (*colored spheres*) that were found to adopt the nearest neighbor position to the OD1 atom of residue D^{127} (drawn as a *stick model*) during any time of their respective trajectories. Residue D^{127} shown here is charged and belongs to monomer M3 (traced in *gray*). All simulated water molecules were considered at 50 ps time intervals to identify these six water molecules. This figure was created using PyMOL (http://pymol.sourceforge.net).

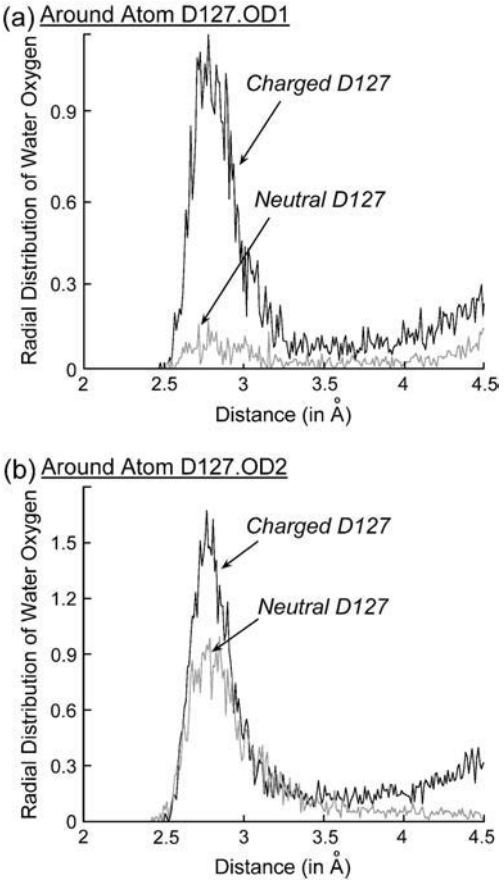

FIGURE 9 Radial distribution of water around the two carboxylate oxygen atoms of residue D^{127} calculated for the last nanosecond trajectory of both simulations: (*a*) around OD1 atom and (*b*) around OD2 atom. Radial distributions were first calculated separately for each monomer and then averaged to obtain single profiles representative of each MD trajectory.

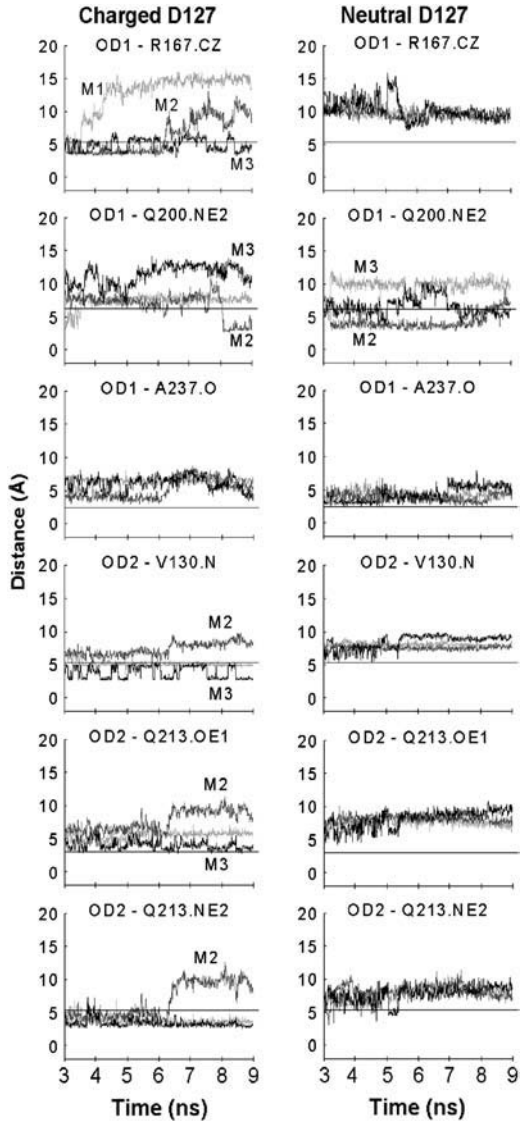

FIGURE 11 Evolution of the local environment of D^{127} in all the six monomers of the two trajectories. The distances of all potential proton donors and acceptors relative to the two carboxylate oxygen atoms of D^{127}, as indicated in Fig. 6, are shown as a function of simulation time. Horizontal lines represent the distance in the crystal structure. The monomers are labeled accordingly only if they are distinguishable from each other.

Together, if we use the crystal data as a reference to determine the protonation state of residue D^{127}, as is normally done in electrostatics-based titration models, a comparison of data between the two trajectories suggests that residue D^{127} is more likely to be charged in the crystal. This is mainly supported by the observations that a), the charged state of D^{127} has a higher tendency to prevent residue R^{167} from moving away from D^{127} and into the channel lumen, and b), the charged state of D^{127} does better at holding water in the positions of the crystallographically resolved waters. However, since we find that the local environment of D^{127} as revealed by the low temperature x-ray structure is not precisely maintained in either trajectory, it seems plausible that under physiological conditions D^{127} might be in either state.

Ion permeation

We observed that cations and anions permeated the channel along different pathways in a screw-like fashion, similar to that observed in several other previous investigations (11,38–40). Fig. 12 shows the time-averaged number of ions at different positions along the length of the pore in both MD trajectories. In both cases, we find cations to have a moderately higher tendency to occupy the pore than anions, corresponding to the known moderate preference of cation-over-anion conduction through the channel (for the most recent review, see Nikaido (8)). In both cases, we find that the bulk of the difference between potassium and chloride ion occupancy is at and around the constriction zone of the channel. The most distinctive difference in the curves for the different protonation states is that for the charged D^{127}, there are two distinct preferred occupancy sites that appear selective

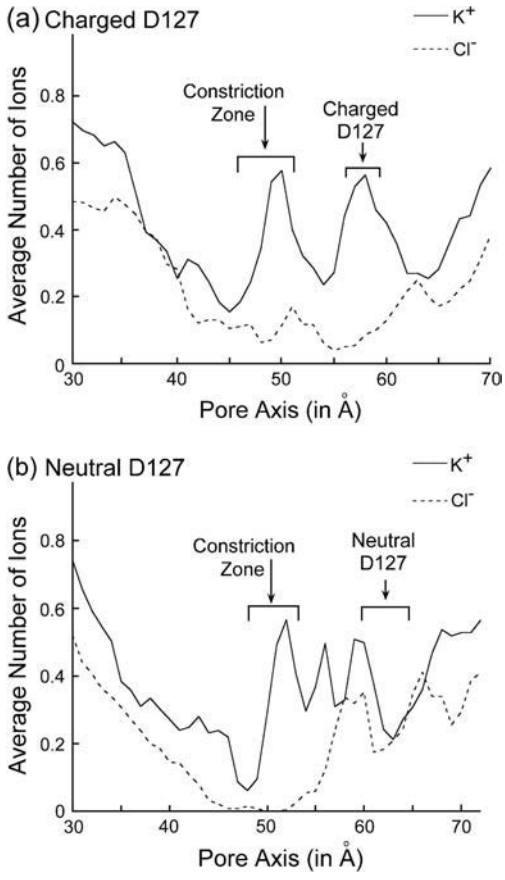

FIGURE 12 Average number of ions along the axis of the two trimers: (*a*) charged D^{127} and (*b*) neutral D^{127}. Positions of the constriction zone and residue D^{127} along the axis of the channel are shown. Irrespective of the protonation state of residue D^{127}, there are moderately greater numbers of potassium than chloride ions in the pore, corresponding to the observed selectivity for potassium over chloride conduction in this channel.

for potassium. Before doing the simulations, we wondered if the potassium selectivity might depend on whether D^{127} was charged, but Fig. 12 shows that this is not the case; the selectivity is maintained in either case. However, this dependency of ion distribution profiles on charges of single residues suggests a basis for changes seen in reversal potentials when charge altering point mutations are introduced (for example, see Phale et al. (40), Van Gelder et al. (41), Samartzidou and Delcour (42), Bredin et al. (43), and Nestorovich et al. (44)), a subject we anticipate will be explored in future studies.

SUMMARY AND CONCLUSIONS

The specific conclusions we draw about the system studied in this work are:

1. Results of the MD simulations and their analysis presented in this work confirmed the hypothesis that use of protonation states computed by Varma and Jakobsson (15) result in agreement between the cross-sectional areas of the constriction zone in the crystal structure of OmpF and unconstrained MD, with residue D^{127} either charged or neutral.
2. Both protonation states of residue D^{127}, charged or neutral, predict moderate selectivity of potassium over chloride in agreement with experiment.
3. In the 310 K simulations presented in this work, there were no systematic dependencies of the backbone structure dynamics of OmpF on the protonation state of residue D^{127}. The side-chain configurations, hydrogen bonding patterns, and hydration patterns seen in the local environment of residue D^{127} were somewhat different from the corresponding configurations and pattern seen in the crystal structure at 77 K. For the neutral D^{127}, the interatomic distances remained essentially unchanged during the simulation after equilibration, whereas for the charged D^{127}, the side chain conformations continued to undergo transitions throughout the simulation. Water radial distribution functions showed that the neutral D^{127} had close interactions with just one water molecule, whereas the charged D^{127} was usually interacting closely with two water molecules. Conclusions about the detailed interaction network of the side chains and water are subject to two caveats: a), It has recently been shown that classical force fields do not give accurate results for the hydration of carboxylate groups (45). Therefore conclusions based in part on simulating this type of interaction should be reconsidered in the future with better force fields. b), And the model we use for protonation states of residues is static. For residues such as D^{127} in OmpF, where there is a close balance between influences tending toward protonation and deprotonation, it would be more realistic to construct a dynamical model for protonation, where a proton could exchange between a residue and water in the course of a simulation.
4. Based primarily on our finding shown in Fig. 8 that the uncharged D^{127} cannot keep the R^{167} side chain from swinging out into the channel lumen, we conclude that D^{127} is probably charged in the low temperature crystal structure. However, under physiological conditions, it seems plausible that D^{127} can exist in both the charged and the uncharged states, and thus switch dynamically between the two states. This hypothesis is reinforced by the results in Fig. 10, which demonstrate that there is frequent exchange of waters in the vicinity of D^{127}, and hence ample opportunity for protonation-deprotonation reactions.
5. These simulations point out a limitation of electrostatics-based titration models in which the dielectric constant of the protein is set at a fixed value. (For a similar point with respect to permeation models, see Allen et al. (46)). Indeed, it is hard to see how any continuum dielectric model, even one that allows for anisotropy and spatial variation, can capture the behavior of polarizable groups in the vicinity of D^{127}, as shown in Fig. 11. We see by the increased mobility of the polar groups in the vicinity of the charged D^{127} that the local apparent polarizability of the channel protein is variable in response to the protonation state of D^{127}. Furthermore, we also see by the increased hydration of charged D^{127} that the polarizability of the cavity associated with penetration of water is also a function of the protonation state of D^{127}. However, we find that the changes in the hydration number of D^{127} are coupled to the changes in interaction of D^{127} with the protein. We see from Fig. 8 *b* that when D^{127} is neutral, its protonated side-chain carboxylate is closely coordinated with the backbone carbonyl of R^{167}. In essence, we see in this polar cavity that the polarizability of the local protein charge groups, the degree of penetration of water, and the protonation state of D^{127} all seem to be very tightly coupled to each other. This is somewhat different from what was seen for the case of introducing a charged residue into a nonpolar cavity (23), where the increase in the local polarizability was essentially exclusively due to increased protein disorder.

The more general inferences we draw from these conclusions are:

1. When considering a situation where multiple charged residues interact with each other, it is important to consider exhaustively the combinatorics of possible interactions, and the range of plausible parameters in Poisson-Boltzmann calculations, when assigning protonation states.
2. Side chain configurations and hydration patterns seen in low-temperature crystals may not reflect the array of configurations experienced in physiological-temperature dynamics.
3. To fully understand the protonation states of titratable residues in proteins, it is necessary to modify the view that the protonation state is determined by the protein

dielectric properties. One may consider instead that the protonation state of a residue and the protein dielectric properties near the residue each affect the other.

Future work suggested by the results of this work include:

1. Similar calculations on the numerous mutants of OmpF for which structures are known to validate the capability of describing in atomistic detail the functional changes associated with mutations. In the longer term, the ultimate goal would be to combine the very compute-intensive MD simulations of the sort described in this work with a more coarse-grained and a less compute-intensive simulation technique. Candidate coarse-grained approaches include transport Monte Carlo (12,47), continuum Poisson-Nernst-Planck theory (48), or Brownian dynamics (49–52). In this strategy, the MD simulations would be used to validate the detailed description of the system. The detailed description of the system would be used to parameterize the much less compute-intensive Brownian dynamics or transport Monte Carlo, which in turn could be used to do sufficiently long simulations that the physiology of the channel could be predicted. Such a capability could be used to develop a computer-aided design capability for reengineering β-barrel channel proteins as conducting components of nanodevices, as postulated by Bayley and Jayasinghe (53).
2. Work on force field improvement to more confidently characterize hydrogen bonding and hydration patterns in side chains.
3. Development of a dynamical protonation/deprotonation model to more confidently characterize this aspect of protein-water interactions.
4. Experimental comparison between side-chain configurations in OmpF at low and physiological temperatures.

SUPPLEMENTARY MATERIAL

An online supplement to this article can be found by visiting BJ Online at http://www.biophysj.org.

We gratefully acknowledge computational time from the National Computational Science Alliance. We also thank all our lab members for their helpful comments and discussions.

This work was supported by National Institutes of Health grant R01GM054651-08 and by the U.S. Dept. of Energy's Genomics: GTL program (www.doegenomestolife.org) under project ''Carbon Sequestration in *Synechococcus Sp.*: from Molecular Machines to Hierarchical Modeling'' (www.genomes-to-life.org).

REFERENCES

1. Nikaido, H., and E. Y. Rosenberg. 1983. Porin channels in Escherichia coli: studies with liposomes reconstituted from purified proteins. *J. Bacteriol.* 153:241–252.
2. Jap, B. K., and P. J. Walian. 1990. Biophysics of the structure and function of porins. *Q. Rev. Biophys.* 23:367–403.
3. Nikaido, H. 1993. Transport across the bacterial outer membrane. *J. Bioenerg. Biomembr.* 25:581–589.
4. Schulz, G. E. 1996. Porins: general to specific, native to engineered passive pores. *Curr. Opin. Struct. Biol.* 6:485–490.
5. Delcour, A. H. 1997. MiniReview: function and modulation of bacterial porins: insights from electrophysiology. *FEMS Microbiol. Lett.* 151:115–123.
6. Schirmer, T. 1998. General and specific porins from bacterial outer membranes. *J. Struct. Biol.* 121:101–109.
7. Koebnik, R., K. P. Locher, and P. V. Gelder. 2000. Structure and function of bacterial outer membrane proteins: barrels in a nutshell. *Mol. Microbiol.* 37:239–253.
8. Nikaido, H. 2003. Molecular basis of bacterial outer membrane permeability revisited. *Microbiol. Mol. Biol. Rev.* 67:593–656.
9. Cowan, S. W., T. Schirmer, G. Rummel, M. Steiert, R. Ghosh, R. A. Pauptit, J. N. Jansonius, and J. P. Rosenbusch. 1992. Crystal structures explain functional properties of two E. coli porins. *Nature.* 358: 727–733.
10. Tieleman, D. P., and H. J. Berendsen. 1998. A molecular dynamics study of the pores formed by Escherichia coli OmpF porin in a fully hydrated palmitoyloleoylphosphatidylcholine bilayer. *Biophys. J.* 74: 2786–2801 [see comments.].
11. Im, W., and B. Roux. 2002. Ions and counterions in a biological channel: a molecular dynamics simulation of OmpF porin from Escherichia coli in an explicit membrane with 1 M KCl aqueous salt solution. *J. Mol. Biol.* 319:1177–1197.
12. van der Straaten, T., S. Varma, S. W. Chiu, J. Tang, N. R. Aluru, R. S. Eisenberg, U. Ravaioli, and E. Jakobsson. 2002. Combining computational chemistry and computational electronics to understand protein ion channels. *ICCN.* 2:60–63.
13. Douglas, J. T., E. Y. Rosenberg, H. Nikaido, D. R. Verstreate, and A. J. Winter. 1984. Porins of Brucella species. *Infect. Immun.* 44:16–21.
14. Rostovtseva, T. K., E. M. Nestorovich, and S. M. Bezrukov. 2002. Partitioning of differently sized poly(ethylene glycol)s into OmpF porin. *Biophys. J.* 82:160–169.
15. Varma, S., and E. Jakobsson. 2004. Ionization states of residues in OmpF and mutants: effects of dielectric constant and interactions between residues. *Biophys. J.* 86:690–704.
16. Karshikoff, A., V. Spassov, S. W. Cowan, R. Ladenstein, and T. Schirmer. 1994. Electrostatic properties of two porin channels from *Escherichia coli*. *J. Mol. Biol.* 240:372–384.
17. Alcaraz, A., E. M. Nestorovich, M. Aguilella-Arzo, V. M. Aguilella, and S. M. Bezrukov. 2004. Salting out the ionic selectivity of a wide channel: the asymmetry of OmpF. *Biophys. J.* 87:943–957.
18. Simonson, T. 1999. Dielectric relaxation in proteins: microscopic and macroscopic models. *Int. J. Quantum Chem.* 73:45–57.
19. Schutz, C. N., and A. Warshel. 2001. What are the dielectric ''constants'' of proteins and how to validate electrostatic models? *Proteins.* 44:400–417.
20. Ullmann, M. G., and E.-W. Knapp. 1999. Electrostatic models for computing protonation and redox equilibria in proteins. *Eur. Biophys. J.* 28:533–551.
21. Antosiewicz, J., J. M. Briggs, A. H. Elcock, M. K. Gilson, and J. A. McCammon. 1996. Computing the ionization states of proteins with a detailed charge model. *J. Comput. Chem.* 17:1633–1644.
22. Fitch, C. A., D. A. Karp, K. K. Lee, W. E. Stites, E. E. Lattman, and E. B. Garcia-Moreno. 2002. Experimental pKa values of buried residues: analysis with continuum methods and role of water penetration. *Biophys. J.* 82:3289–3304.
23. Denisov, V. P., J. L. Schlessman, E. B. Garcia-Moreno, and B. Halle. 2004. Stabilization of internal charges in a protein: water penetration or conformational change? *Biophys. J.* 87:3982–3994.
24. Dwyer, J. J., A. G. Gittis, D. A. Karp, E. E. Lattman, D. S. Spencer, W. E. Stites, and E. B. Garcia-Moreno. 2000. High apparent dielectric constants in the interior of a protein reflect water penetration. *Biophys. J.* 79:1610–1620.

25. Lindahl, E., B. Hess, and D. v. d. Spoel. 2001. GROMACS: a package for molecular simulation and trajectory analysis. *J. Mol. Model.* 7: 306–313.

26. Hess, B., H. Bekker, H. J. Berendsen, and G. E. M. Fraaije. 1997. LINCS: a linear constraint solver for molecular simulations. *J. Comput. Chem.* 18:1463–1472.

27. Miyamoto, S., and P. Kollman. 1992. SETTLE: an analytical version of the SHAKE and RATTLE algorithms for rigid water molecules. *J. Comput. Chem.* 13:952–962.

28. Hoover, W. G. 1985. Canonical dynamics: equilibrium phase-space distributions. *Phys. Rev. A.* 31:1695–1697.

29. Parrinello, M., and A. Rahman. 1981. Polymorphic transition in single crystals: a new molecular dynamics method. *J. Appl. Phys.* 52:7128–7190.

30. van Gunsteren, W. F., S. R. Billeter, R. A. Eising, P. H. Hünenberger, P. Krüger, A. E. Mark, W. R. P. Scott, and I. G. Tironi. 1996. Biomolecular Simulation: The GROMOS96 Manual and User Guide. Hochschulverlat an der ETH Zürich/Biomos, Zürich/Groningen, The Netherlands.

31. Reference deleted in proof.

32. Smart, O. S., J. M. Goodfellow, and B. A. Wallace. 1993. The pore dimensions of gramicidin A. *Biophys. J.* 65:2455–2460.

33. Smart, O. S., J. G. Neduvelila, X. Wanga, B. A. Wallacea, and M. S. Sansom. 1996. HOLE: a program for the analysis of the pore dimensions of ion channel structural models. *J. Mol. Graph.* 14:354–360.

34. Pauptit, R. A., H. Zhang, G. Rummel, T. Schirmer, J. N. Jansonius, and J. P. Rosenbusch. 1991. Trigonal crystals of porin from Escherichia coli. *J. Mol. Biol.* 218:505–507.

35. Jeanteur, D., J. H. Lakey, and F. Pattus. 1991. The bacterial porin superfamily: sequence alignment and structure prediction. *Mol. Microbiol.* 5:2153–2164.

36. Liu, N., and A. H. Delcour. 1998. The spontaneous gating activity of OmpC porin is affected by mutations of a putative hydrogen bond network or of a salt bridge between the L3 loop and the barrel. *Protein Eng.* 11:797–802.

37. Bainbridge, G., H. Mobasheri, G. A. Armstrong, E. J. A. Lea, and J. H. Lakey. 1998. Voltage-gating of Escherichia coli porin: a cystine-scanning mutagenesis study of loop 3. *J. Mol. Biol.* 275:171–176.

38. Suenaga, A., Y. Komeiji, M. Uebayasi, T. Meguro, M. Saito, and I. Yamato. 1998. Computational observation of an ion permeation through a channel protein. *Biosci. Rep.* 18:39–48.

39. Schirmer, T., and P. S. Phale. 1999. Brownian dynamics simulation of ion flow through porin channels. *J. Mol. Biol.* 294:1159–1167.

40. Phale, P. S., A. Philippsen, C. Widmer, V. P. Phale, J. P. Rosenbusch, and T. Schirmer. 2001. Role of charged residues at the OmpF porin channel constriction probed by mutagenesis and simulation. *Biochemistry.* 40:6319–6325.

41. Van Gelder, P. V., N. Saint, P. S. Phale, E. F. Eppens, A. Prilipov, R. v. Boxtel, J. P. Rosenbusch, and J. Tommassen. 1997. Voltage sensing in the PhoE and OmpF outer membrane porins of *Escherichia coli*: role of charged residues. *J. Mol. Biol.* 269:468–472.

42. Samartzidou, H., and A. H. Delcour. 1999. Distinct sensitivities of OmpF and PhoE porins to charged modulators. *FEBS Lett.* 444:65–70.

43. Bredin, J., N. Saint, M. Mallea, E. D. G. Molle, J. M. Pages, and V. Simonet. 2002. Alteration of pore properties of *Escherichia coli* OmpF induced by mutation of key residues in anti-loop 3 region. *Biochem. J.* 363:521–528.

44. Nestorovich, E. M., T. K. Rostovtseva, and S. M. Bezrukov. 2003. Residue ionization and ion transport through OmpF channels. *Biophys. J.* 85:3718–3729.

45. Leung, K., and S. B. Rempe. 2004. Ab initio molecular dynamics study of formate ion hydration. *J. Am. Chem. Soc.* 126:344–351.

46. Allen, T. W., O. S. Andersen, and B. Roux. 2004. On the importance of atomic fluctuations, protein flexibility, and solvent in ion permeation. *J. Gen. Physiol.* 124:679–690.

47. Graf, P., A. Nitzan, M. G. Kurnikova, and R. D. Coalson. 2000. A dynamic lattice Monte Carlo model of ion transport in inhomogeneous dielectric environments. Method and Implementation. *J. Phys. Chem. B.* 104:12324–12338.

48. van der Straaten, T., J. M. Tang, U. Ravaioli, R. S. Eisenberg, and N. R. Aluru. 2003. Simulating ion permeation through the ompF porin ion channel using three-dimensional drift-diffusion theory. *J. Comput. Electronics.* 2:29–47.

49. Cooper, K., E. Jakobsson, and P. Wolynes. 1985. The theory of ion transport through membrane channels. *Prog. Biophys. Mol. Biol.* 46: 51–96.

50. Im, W., S. Seefeld, and B. Roux. 2000. A grand canonical Monte Carlo-Brownian dynamics algorithm for simulating ion channels. *Biophys. J.* 79:788–801.

51. Mashl, R. J., Y. Tang, J. Schnitzer, and E. Jakobsson. 2001. Hierarchical approach to predicting permeation in ion channels. *Biophys. J.* 81:2473–2483.

52. Chung, S. H., M. Hoyles, T. Allen, and S. Kuyucak. 1998. Study of ionic currents across a model membrane channel using Brownian dynamics. *Biophys. J.* 75:793–809.

53. Bayley, H., and L. Jayasinghe. 2004. Functional engineered channels and pores (Review). *Mol. Membr. Biol.* 21:209–220.